Front. Earth Sci. 2023, 17(1): 87–99
https://doi.org/10.1007/s11707-021-0967-4

RESEARCH ARTICLE

The evolution of coal, examining the transitions from anthracite to natural graphite: a spectroscopy and optical microscopy evaluation

Liang YUAN[1], Qinfu LIU (✉)[1], Kuo LI[1], Ying QUAN[1], Xiaoguang LI[2], Jonathan P. MATHEWS[3]

1 School of Geosciences and Surveying Engineering, China University of Mining and Technology (Beijing), Beijing 100083, China
2 State Key Laboratory of Lithospheric Evolution, Institute of Geology and Geophysics, Chinese Academy of Sciences, Beijing 100029, China
3 The EMS Energy Institute, and the Leone Family Department of Energy and Mineral Engineering, Pennsylvania State University, University Park PA 16802, USA

Abstract Coal-derived natural graphite (CDNG) has multiple industrial applications. Here, ten metamorphic coals from anthracite to CDNG were obtained from Lutang and Xinhua in the Hunan Province and Panshi in the Jilin Province. Bulk characterization (proximate and ultimate analyses, X-Ray powder diffraction (XRD), and powder Raman spectroscopy), along with optical microscopy, scanning electron microscope (SEM) and micro-Raman spectroscopy were utilized to examine the transitions from anthracite to semi-graphite to CDNG. The XRD and Raman spectroscopy data indicate that from anthracite to highly ordered graphite the average crystal diameter (L_a) and height (L_c) increased from 6.1 and 4.6 nm to 34.8 and 27.5 nm, respectively. The crystalline parameters of the CDNG samples from Panshi and Lutang varied slightly when closer to the intrusive body. Optical microscopy and SEM indicated that in the anthracite samples there were thermoplastic vitrinite, devolatilized vitrinite, and some "normal" macerals. In the meta-anthracite, pyrolytic carbon, mosaic structure, and crystalline tar were present. In the CDNG there were flake graphite, crystalline aggregates, and matrix graphite. The crystalline aggregates show the highest structural ordering degree as determined from Raman spectral parameters (full-width at half maxima (G-FWHM) ~20 cm^{-1}, D1/(D1 + D2 + G) area ratio (R2) value < 0.5). The flake graphite is less ordered with G-FWHM ~28 cm^{-1} and 0.5 < R2 < 1, but a larger grain size (up to 50 μm). The mosaic structures were likely the precursors of the matrix graphite through *in situ* solid-state transformation. The pyrolytic carbon and crystalline tars are the transient phase of gas-state and liquid-state transformations. This study is beneficial to realize the rational utilization of CDNG.

Received December 17, 2021; accepted January 4, 2022

E-mail: lqf@cumtb.edu.cn

Keywords micro-Raman spectroscopy, structural ordering evolution, coal-derived natural graphite, XRD, anthracite

1 Introduction

The world has 60 Mt of microcrystalline graphite reserves, of which China holds 55 Mt (Robinson et al., 2017). The coal-derived natural graphite (CDNG) in China belongs to the microcrystalline graphite and is 60% of the domestic reserves (Li, 2019). Owing to its high carbon content, availability, and easy exploration, there are considerable commercial opportunities due to the rapid depletion of flake graphite reserves (Wang et al., 2019b). However, as the CDNG coexists with anthracite, which lacks effective methods to distinguish, it is often burned like coal, causing a huge waste of resources. Additionally, the graphitization process of different macerals is different, but related research remains elusive. As graphite plays an important role in the new energy revolution, getting a better understanding of the coal natural graphitization process will enhance the CDNG utilization value.

Graphitization needs graphitizable carbons (Beyssac and Rumble, 2014; Harris, 2005), sufficient heat (Buseck and Beyssac, 2014; Oberlin, 1984), adequate pressure (Bonijoly et al., 1982), and perhaps some catalysts (Buseck and Huang, 1985; Duber et al., 1993). The CDNG is usually formed in a metamorphic belt associated with igneous intrusion and tectonic stress. Igneous intrusions and tectonic movements made the coal metamorphic, forming metamorphic aureole transforming coal from anthracite to CDNG. The coal closer to the magma intrusion will have been exposed to higher temperatures

and experience a longer heating duration (Yuan et al., 2021). Tectonic stress can also facilitate graphitization. Strain stress can change the coals' molecular structure directly. The local stress concentration promotes the preferred orientations of the local basic structural units (BSUs) and removes structural defects, leading to the gradual expansion of locally ordered structures (Wang et al., 2019a). The kinetic energy of tectonic stress can be converted into heat through friction (Kuo et al., 2014; Wang et al., 2014). Thus, anthracite is thought to be the main precursor of the CDNG due to its well-aligned aromatic structure. Anthracite has a better graphitizability than other graphitizing carbons when the temperature is > 2000°C in synthetic graphitization (Oberlin and Terriere, 1975). However, the temperature required for natural graphitization is only 300°C–500°C (Buseck and Huang, 1985; Bustin et al., 1995), which is much lower than that of synthetic graphitization. The ability of anthracites to graphitize has been related to the characteristics, such as the initial spatial arrangement of BSUs. Some anthracites give rise to carbon that have mainly a graphitic structure, whereas others produce porous and turbostratic carbons (Blanche et al., 1995). The maceral groups also influence the graphitization: vitrinite is more graphitizable than inertinite (Wang et al., 2019b). Besides these factors, the amount, type, and distribution of mineral matter have been shown to facilitate (González et al., 2003) or inhibit (Nyathi et al., 2013) graphitization.

In graphitization, the structural ordering evolution in the microscale has been detailed through direct observation from HRTEM micrographs (Buseck and Huang, 1985; Oberlin and Terriere, 1975; Zheng et al., 1996). These can be summarized as anthracite having poorly organized aromatic rings stacked within five layers and extended within 2 nm width, forming a BSU. In the meta-anthracite, these BSUs aligned along a preferential direction to form local molecular orientation domains and the local molecular orientation domain tends to coalescence forming an oriented domain (Li et al., 2020a; Li et al., 2021). With the metamorphic degree increasing, the curvature and structure defects of coal molecules were removed, thus forming highly ordered graphite (Li et al., 2020a). Our previous work quantified this process (Yuan et al., 2021), what remains elusive is the transitions within the microscopically distinguishable components (MDC). Hower et al. (2021a) found that the metamorphism of anthracites (typically the Cretaceous Cerrillos anthracite, Butte anthracites, and the Pennsylvania anthracites) differs from the metamorphism of breccia (typically the Ragged Edge breccia). The Cretaceous Cerrillos and Crested Butte anthracites were both metamorphosed by igneous intrusions, but not in close enough proximity to producing natural coke. For Pennsylvania anthracites, the hydrothermal mineralizing fluids at >375°C and >22 MPa driven up the rank of coal from high volatile C or B bituminous-rank level to anthracite. Hower et al. (2021b) also pointed out that the duration of the heating, melting, and resolidification event was about 1 h based on the known behavior vitrinite at high temperatures and, to a lesser extent, at high pressures.

X-ray diffraction (XRD) provides average structure information (i.e., crystalline diameter (L_a), crystalline height (L_c), average layers (N_{ave})). Petrographic analyses give information of reflectance, morphological features, and interference colors, aided in distinguishing different MDC types. The micro-Raman spectroscopy uses a microscope permitting analyses of specific components, besides micro-Raman spectroscopy of coal allows obtaining the Raman spectrum of a selective volume of material, with a lateral resolution > 1 μm. Thus, it enables the analysis of specific macerals/MDC. Previously, micro-Raman spectroscopy has been performed in various macerals up to anthracite rank (Guedes et al., 2010 and 2012). Rantitsch et al. (2016) characterized graphite and semi-graphite samples from several mines worldwide by the D1/(D1 + D2 + G) area ratio (R2) and the full-width at half maxima of G band (G-FWHM), the obtained microstructural data suggest a continuous transformation of semi-graphite enclosed in lower greenschist-facies rocks to graphite from amphibolite- to granulite-facies rocks. Kwiecinska et al. (2010) use micro-Raman to quantify the crystallographic structure and the differences between the meta-anthracite, semi-graphite, and graphite.

The harsh CDNG deposit setting makes the CDNG a unique graphite resource worldwide. The currently mining CDNG deposit in China mainly occurs in Xinhua and Lutang, Hunan Province, and Panshi, Jilin Province. Previous studies have focused on anthracite/graphite from the same metamorphic aureole with different maturation (Li et al., 2018 and 2019). However, samples collected from the single area do not cover all the metamorphic phases. Here, we selected samples from three typical CDNG deposits: Xinhua, Panshi, and Lutang. The CDNG in these three regions accounts for 94% of total China's CDNG reserve (Li, 2019) and covers each transitional phase throughout the metamorphic process, thus capturing the CDNG processes.

2 Geological settings

Figure 1 shows the sampling locations. The Xinhua mining areas are located in the Lianyuan Basin in the central Hunan Province. The coal-bearing strata are within the lower Carboniferous Ceshui Formation (earlier than 290 Ma). The samples CM, SL, BC, and SXL were collected in the Choumu, Shenli, Baicong, and Shixiangli mines, toward the Tianlongshan granitic pluton with distances of 2.0, 1.1, 0.6, and 0.3 km. The age of the

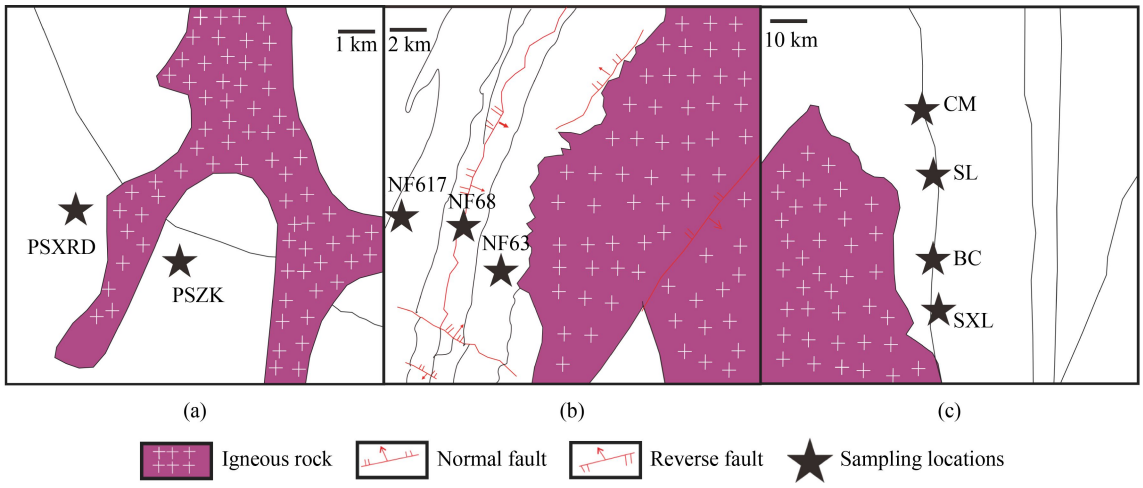

Fig. 1 Geological sketch map of the study region showing sampling locations (the Xinhua area was modified after (Li et al., 2018) and the Lutang area was modified after (Wang et al., 2019a)). (a) Panshi, Jilin Province, (b) Lutang, Hunan Province, and (c) Xinhua, Hunan Province.

granite is ~202–208 Ma. All of these samples are collected in the No. 3 coal seam. Coal strata in the area closest to the pluton are deformed and seams are nearly vertical.

The Lutang mining areas are located in the southwest of Hunan Province, which lies between the Cathaysia and the Yangtze Blocks. The tectonic and magmatic activities were most intense during the Indosinian-Yanshanian Period (135–233 Ma) (Huang, 2005). The Qitianling granitic pluton intruded east of the research area during the Yanshanian period (146–163 Ma) (Zhu et al., 2009), covering an area of 530 km^2. The coal-bearing strata occurred in the upper Permian Longtan Formation. The metamorphism gradually decreases with increasing distance from the pluton (Chao et al., 2017). The study area is divided into three zones near the intrusion: the chlorite zone (700–1300 m, 300°C–450°C), the biotite zone (400–700 m, 400°C–500°C), and the hornfels zone (0–400 m, 450°C–600°C) (Wang et al., 2019a; Wu et al., 2021). The main tectonic structure in the area is the NNE-striking Lutang–Shatian syncline. The western flank manifests as broad and gentle folds, while structures at the eastern flank are characterized by tight folds. The samples were collected in Nanfang No. 6 mine (NF63, NF68, and NF617). Their distance to the Qitianling granitic pluton was 0.5, 1.5, and 3.0 km, respectively.

The Panshi mining areas are located in the central part of Jilin Province, between the Dunmi fault zone and the Lamulun fault zone, covering an area of 25 km^2 and the coal seam was highly altered during the Yanshanian Period (Yuan et al., 2021). The PSZK and PSXRD were sampled in the Zhang, and Xianrendong mines, respectively, where coal-bearing strata occurred in the Triassic Dajianggang Formation. The distances to the intrusion body were 0.6 and 0.9 km.

3 Samples and methods

3.1 Sample preparation

The powdered samples (−200 mesh) were used for proximate analyses. A three-step HCl-HF demineralization process was performed, using 5 g of the sample dispersed in 30 mL of HCl solution (37 wt%) and 20 mL of HF solution (40 wt%); with stirred for 12 h. This process was performed sequentially three times. The samples were filtered and washed with deionized water until the pH value was 7. Samples were filtered and dried in a muffle furnace at 60°C for 12 h. The acid-treat samples were used for XRD.

The samples were crushed to −20 mesh and pulverized to −200 mesh. The crushed samples (−20 mesh) were mixed with epoxy resin to make pellets for petrographic analyses and micro-Raman spectroscopic analysis. The pellets were allowed to cure and were polished using a Buehler Autonet 250.

3.2 Analytical methods

3.2.1 Proximate and ultimate analyses

The proximate and ultimate analyses were conducted per ASTM standard D3172-13 and ASTM standard D5373-14, respectively. These analyses were conducted at the Shanxi Institute of Geology and Mineral Resources.

3.2.2 XRD

The acid-treat powder samples were analyzed using a Rigaku D/max-2500 PC diffractometer equipped with Cu Ka radiation. The X-ray generator voltage and current were constant at 40 kV and 100 mA. The sample was

scanned using the continuous sweep method from 2.5° to 80° (in the 2θ range) at a rate of 2°/min. The XRD test was conducted at the China University of Mining & Technology, Beijing.

Three detected peaks were the π-band (002), γ-band (left π-band), and the (100) band (around 43°) (Lu et al., 2001). To quantify the structural evolution, peak-fitting using the pseudo-Voigt function in the Jade 5 package was applied. For the crystal structure parameters: interlayer spacing (d_{002}), crystallite height (L_c), crystallite diameter (L_a), and average stacked aromatic layers (N_{ave}) were calculated using the Scherrer equations: $L_a=1.84\lambda/\beta_a\cos(\theta_a)$; $L_c=0.89\lambda/\beta_c\cos(\theta_c)$; $N_{ave}=L_c/d_{002}+1$.

Here, λ is the wavelength (0.154056 nm) of the radiation; β_a and β_c are the FWHM of the (002) and (10) peaks, respectively, and θ_a and θ_c are their corresponding Bragg angles.

For better characterizing the structural ordering evolution after entering the meta-anthracite stage, the *AI* (Asymmetric index of the (002) band) was adopted per Zhang et al. (2020). As the turbostratic structure and structural defects cause the γ band, resulting in the asymmetry of the (002) band. Therefore, the *AI* value can evaluate the structural ordering. The *AI* can be detailed as follows (Fig. 2). $AI = \gamma_1 / \gamma_2$.

3.2.3 Petrographic analyses

The R_{max} value was measured using a CRAIC Coal-Pro micro-reflectometer coupled with a Leica DM 2500P reflected-light microscope as per the ASTM D2798-11a. For the highly ordered graphite (SXL, NF63, NF68, NF617, PSXRD, and PSZK), Graphite grains were selected for testing reflectance (R_{max}, %) as vitrinite was altered in the CDNG samples. Photomicrographs were taken under white light, oil immersion.

3.2.4 Micro-Raman spectroscopy

The micro-Raman spectrum of samples was collected by a confocal Raman Microscope alpha 300R at WITec GmbH (Ulm, Germany). This system is equipped with a solid-state continuous-wave laser emitting at 532 nm. A piece of single-crystal silicon was used to calibrate the wavenumbers of the shifts. A 50× or 100× (NA = 0.9) ZEISS objective was selected for excitation and detection, and the Rayleigh light was rejected by an edge filter. A 300 grooves/mm grating was used to disperse the light with the spectral resolution of 4.8 cm^{-1}. The laser with a power of 5 mW was focused on the sample, and the acquisition time was 10 s with an accumulation of 2. The micro-Raman tests were conducted in the Institute of Geology and Geophysics, Chinese Academy of Sciences.

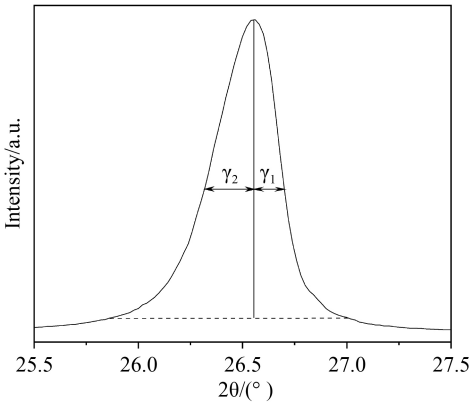

Fig. 2 Illustration of how to calculate asymmetry index (*AI*).

The spectra were analyzed using the Lorentzian curve-fitting procedure in OriginLab 2021 software. In the first-order region, five distinguishing bands were fitted. The G band (~1580 cm^{-1}) is attributed to the E_{2g} vibration mode of carbon rings in graphite sheets, and the D1 band (~1350 cm^{-1}), D2 band (~1620 cm^{-1}), D3 band (~1500 cm^{-1}), and D4 band (~1200 cm^{-1}) are all described as defect-induced bands (Kwiecinska et al., 2010). The D1 band is attributed to the in-plane defects, while the D2 band at the shoulder of the G band is not yet well understood until recently (Schwan et al., 1996). The D3 band and D4 band are separately related to the defects outside the plane and hexagonal diamond or sp^3-rich phase (Hinrichs et al., 2014; Potgieter-Vermaak et al., 2011). For the raw Raman peaks in the second peak region, the $2D_R$ (~2450 cm^{-1}), 2D peak (~2700 cm^{-1}), D1+G peak (~2900 cm^{-1}), and $2D_2$ peak (~3240 cm^{-1}) are often present, they were treated as the overtones and combinations of the disorder-induced bands (Nemanich and Solin, 1979).

Carbonaceous matter can be sensitive to the polishing process, which leads to erroneous Raman spectra of these materials. The samples investigated have been processed by crushing and pulverization. Because mechanical stress from shearing or polishing may influence the Raman spectra, it is necessary to evaluate this potential contributing factor. A highly ordered graphite sample from Sri Lanka was polished and analyzed to determine whether polishing had any effect on the Raman spectra. No defect-induced band was detected in the Raman spectra of the polished Sri Lanka graphite (see the supplementary material), suggesting no adverse effects from the polishing.

3.2.5 Scanning electron microscope (SEM)

The demineralized samples were used for SEM analysis. First, Rotary-pump sputtering was used to coat the pump samples (heights < 0.5 cm and diameters < 1 cm) with an ultra-thin coating of gold to afford a thickness range of 1–2 nm to enhance their electrical conductivity. Then, surface morphology of series samples was analyzed using a Hitachi S-4800 SEM.

4 Results and discussion

4.1 Conventional analyses

Basic coal data are shown in Table 1. All the samples exhibit a high metamorphic degree with a high C content value (> 90%) and low volatile yielding, H (< 0.5%), O (< 5%) content value. The data provided by ultimate analyses varies subtly between samples. In coalification, the loss of the aliphatic side chain will lead to the decrease of H, O content value, while in graphitization, the major structural change is the rearrangement of the C atoms network rather than the loss of aliphatic side chains. The R_{max} value was high for the CM sample and SL sample. However, for the other samples, the R_{max} remains stable at 4%–6%, this is consistent with the previous reported values for naturally graphitized coals (Li et al., 2018). The changes in the size and orientation of the BSU have a contribution to the increase in the vitrinite reflectance, while in graphitization the BSU rearrangement terminated this increase. The BC sample is in graphitization with a low R_{max} value.

4.2 Average crystalline structure

The XRD patterns of the samples are shown in Fig. 3. The CM is classified as coal samples with a board (002) peak within 20°–30° (2θ). From the XRD pattern, with the distance from the coal seam to the igneous rock decrease in the same region, the (002) peak gradually becomes narrower with greater intensity and a smaller FWHM, indicating a better structural ordering is achieved. The Raman spectra exhibited a continued evident ordering from the reduction in the D bands and the emergence of higher intensity, narrower G bands which is consistent with the XRD data.

Detailed crystalline parameters are listed in Table 2. For the structural ordering parameters, the International Committee for Coal and Organic Petrology (ICCP) uses d_{002} value, H/C, and R_{max}% to classify the metamorphic degree above anthracite rank (Kwiecińska and Petersen, 2004). While the vitrinite reflectance is not a valid parameter for highly graphitized coals due to the structural rearrangement of the BSUs (Rantitsch et al., 2016). Unfortunately, as the H content is very low, the H/C ratio cannot be used as a reliable parameter for the CDNG samples, therefore, the only parameter to distinguish the transitional phase is d_{002}.

Here, we use the d_{002} interlayer distance of samples as an ICCP-defined reference. The sample CM is classified as anthracites with their d_{002} values > 0.34 nm. The SL sample with a d_{002} value between 0.338 and 0.34 nm is classified as meta-anthracite, and BC with a d_{002} value between 0.337 and 0.338 nm is classified as semi-graphite. The other samples with d_{002} values ⩽ 0.337 nm are classified as CDNG. The L_a, L_c, and N_{ave} of samples in the Xinhua region increased as the d_{002} interlayer distance decreased. However, for the CDNG samples in Lutang and Panshi, the L_a, L_c, and N_{ave} do not increase with the decreasing d_{002} values as expected. The NF68 sample has the lowest L_c, and N_{ave} in comparison with NF617 and NF63 CDNG samples. The local molecular orientation domains may slip and splice and finally connect under shear stress. As we can see from Fig. 1. The NF68 is sampled near a reverse fault, where direct shear stress made the sample's BSU diameter longer but a short height along with less stacking.

As is shown in Fig. 4. The *AI* has a linear relationship with d_{002}. The samples NF63, NF68, NF617, PSXRD, and PSZK are all classified as highly ordered graphite with their *AI* values > 0.63. As is shown in Table 2, the G-FWHM of the CDNG samples varies slightly. As the

Table 1 Proximate and ultimate analyses (part of data from Yuan et al. (2021) and Li et al. (2018))

Region	Samples	Proximate analysis (wt%)				Ultimate analysis (wt%, dmmf)				Macerals or MDCs
		Moist (ad)	Ash (d)	VM (daf)	FC (d)	C	H	O	R_{max}%	
Xinhua	CM	1.53	2.09	4.29	95.71	94.36	0.87	4.65	9.49	48.2% vitirnite, 51.1% inertinite
	SL	2.38	15.65	5.62	79.6	93.7	0.46	3.41	9.96	37.7% vitrinite, 39.6% inertinite,
	BC	1.84	10.09	4.89	85.51	96.4	0.31	2.86	5.39	17.5% vitrinite, 27.3% Inertinite, 46.6% MG
	SXL	0.68	8.36	5.93	88.8	98.46	0.04	1.17	4.95	4.3% inertinite, 82.6% MG
Lutang	NF63	0.69	12.91	1.69	85.62	97.89	0.06	1.99	6.02	40.3% MG, 23.4% FG, 10% CA
	NF68	0.95	18.83	3.51	78.32	98.33	0.03	3.59	5.29	56.3% MG, 33% FG, 12.4% CA
	NF617	0.81	25.28	3.78	71.89	97.35	0.19	2.21	4.68	70.4% MG, 23.1% FG, 7.4% CA
Panshi	PSXRD	2.22	26.04	3.51	71.36	95.92	0.04	nd	4.54	65.4% MG, 13.3% FG, 20.5% CA
	PSZK	0.86	49.29	6.6	47.29	99.33	nd	nd	5.28	80.1% MG, 12.3% FG, 3% CA

Notes: nd: not detected; ad: as-determined basis; dmmf: dry, mineral matter-free basis; daf: dry ash-free basis; d: dry basis; VM: volatile matter; FC: fixed carbon. MG is matrix graphite, FG is flake graphite, and CA is crystalline aggregates.

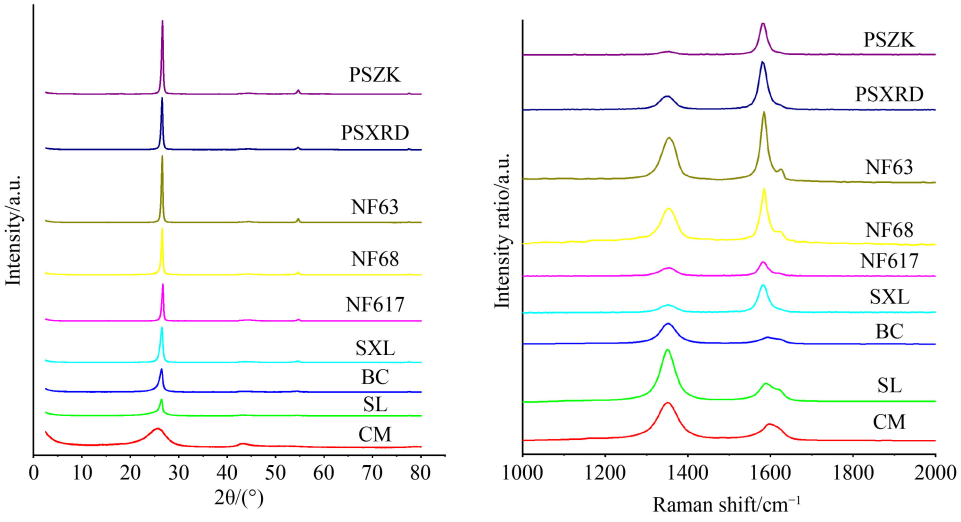

Fig. 3 Raw XRD and Raman spectra of demineralized coal and CDNG samples.

Table 2 Crystalline parameter and basic properties of coal and CDNG

Region	Samples	d_{002}/nm	L_a/nm	$L_c$nm	N_{ave}	AI	R2	G-FWHM (cm^{-1})	Types
Xinhua	CM	0.3476	6.1	4.6	14		0.75	51	anthracite
	SL	0.3381	36.5	19.5	59	0.55	0.62	48	meta-anthracite
	BC	0.3370	23.4	17.2	52	0.47	0.70	40	semi-graphite
	SXL	0.3378	34.8	27.5	83	0.61	0.59	25	CDNG
Lutang	NF63	0.3354	74.5	39.2	117	0.68	0.43	20	CDNG
	NF68	0.3355	88.3	34.4	104	0.65	0.48	20	CDNG
	NF617	0.3367	74.5	39.2	118	0.63	0.60	20	CDNG
Panshi	PSXRD	0.3355	57.4	39.4	118	0.70	0.53	23	CDNG
	PSZK	0.3354	72.2	42.1	127	0.72	0.46	20	CDNG

Notes: N_{ave}: average layers; AI: asymmetric index; R2: D1 / (D1 + D2 + G) area ratio; G-FWHM: full-width at half maxima of G band.

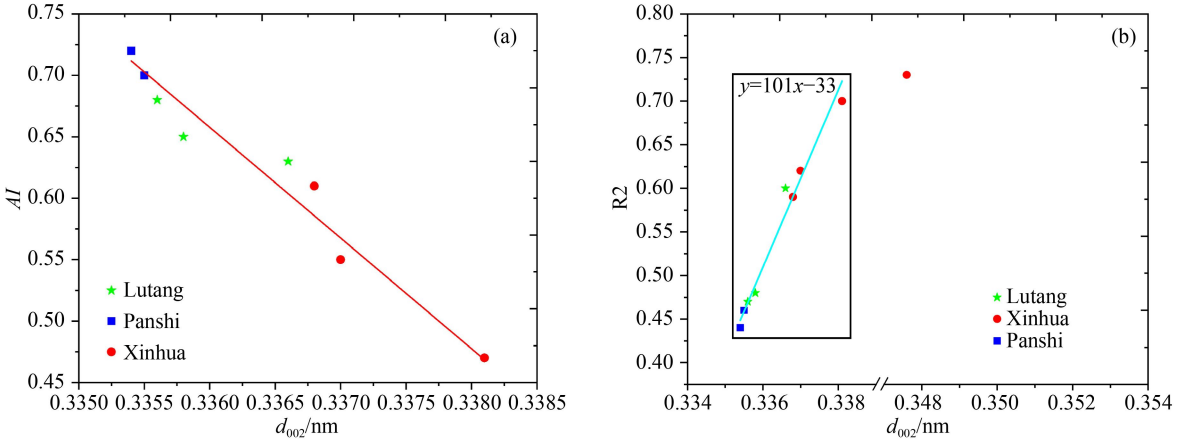

Fig. 4 Relationship between *AI* (a), R2, and d_{002} (b).

predominantly triperiodical structural order is attained (Table 1), a further decrease of the d_{002} parameter results only in a minor decrease of the G-FWHM. The structural defects of graphene and anthracite shared many similarities in Raman spectra (Han et al., 2016). In graphene, the D1/D2 intensity ratio can be used to distinguish the type of structure defects (Eckmann et al., 2012). While the R1 (D1/G intensity ratio), D1/G area ratio, G-FWHM, these parameters do not consider the D2 peak in comparison with R2 make R2 a better parameter

to evaluate the structural order. Figure 3 shows the relationship between the R2 and d_{002}; the R2 value has a better linear relationship with d_{002} after graphitization.

4.3 Morphological features of MDC (via optical microscopy and SEM)

Although the macerals had been altered significantly by igneous intrusion and tectonic stress, some maceral precursors could be identified through microscope. For the less altered anthracite sample CM (R_{max} = 9.49%). The thermoplastic vitrinite (Figs. 5(a)–5(b)), the devolatilized vitrinite (Fig. 5(c)), and some "normal" macerals were present. The "normal" macerals were composed of desmocollinite (Fig. 5(d)). The thermoplastic vitrinite exhibits a weak optical anisotropy as it shows no difference when the microscope platform rotated 90° (Figs. 5(a)–5(b)). No liptinite was found and no preservation of maceral textures of bituminous precursors. The SEM images show that the edge side and frontage side of the graphite sheet with length < 3 μm and heights < 40 nm. These graphite sheets are stacked randomly. Here, the CM anthracite shows a significant difference compared with Pennsylvania anthracite reported before (Hower et al., 2019, 2021a, and 2021b). Hower et al. (2019) suggests that the thermoplastic vitrinite is not an igneous magma and heat alone is not sufficient to keep it in a fluid state based on comparisons between laboratory studies of thermoplasticity of vitrinite and the natural conditions.

For the representative meta-anthracite sample SL (R_{max} = 9.96%), the major of the MDC are the thermoplastic vitrinite. Besides, some newly formed components were present include pyrolytic carbon, mosaic structure, and crystalline tar. The pyrolytic carbon occurs along the edges of the brecciated fragments (Fig. 6(a)), which are the deposits formed on a hot substrate by dehydrogenation of a gaseous hydrocarbon (Kwiecińska and Pusz, 2016; Oberlin, 2002). The presence of pyrolytic carbon, both in vitrinite cavities, at the edge of the melted zone, and in fractures suggests a gas phase associated with the melting event (Goodarzi et al., 1992). The mosaic structure (Fig. 6(b)) lacks a clear outline between other macerals or MDC as a result of the local softening and melting of the "normal" macerals. The mosaic structure has been identified similar features as

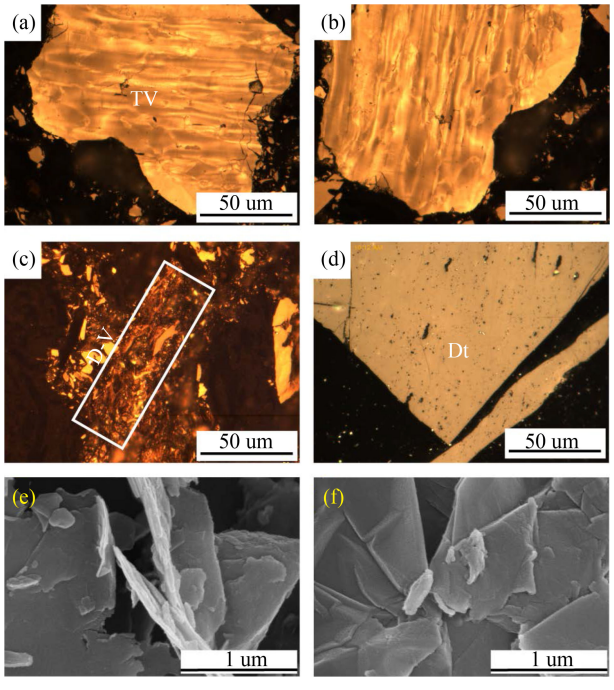

Fig. 5 Representative photomicrographs and SEM images of samples. For optical observation, the images were taken under polarized light, × 50 anti-reflective objective, under oil immersion. (a) thermoplastic vitrinite (TV); (b) TV with 90° rotation; (c) devolatilized vitrinite (D-V); (d) desmocollinite (Dt); (e) edge side of the graphite sheet under SEM and (f) frontage of the graphite sheet under SEM.

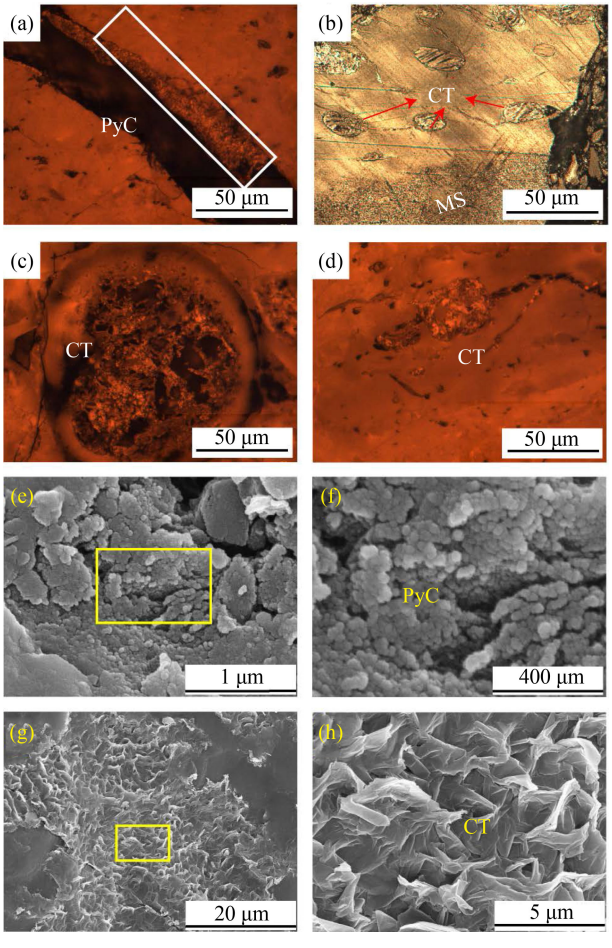

Fig. 6 Representative photomicrographs and SEM of samples. For optical observation, the images were taken under polarized light, × 50 anti-reflective objective, under oil immersion. (a) Pyrolytic carbon (PyC); (b) crystalline tar (CT) and mosaic structure (MS); (c) CT in the cell cavity; (d) CT in the fracture; (e) PyC under SEM; (f) a focus on the PyC microspheres of (e); (g) CT under SEM; (h) a focus on the CT of (g).

microcrystalline graphite (Li et al., 2018). The crystalline tar exhibits a lamellar structure which is also called needle-like graphite or silk-like graphite in some articles (Li et al., 2018 and 2019; Wang et al., 2019b). It usually formed in the void cavities such as cells (Figs. 6(b)–6(c)) or fractures (Fig. 6(d)). Per the SEM, the pyrolytic carbon (Figs. 6(e) –6(f)) presents some microspheres (20–40 nm) agglomerate. These microspheres are much smaller in size than the pyrolytic carbon reported previously in synthetic graphitization (1–10 μm) (Oberlin, 2002) while the crystalline tar (Figs. 6(g)–6(h)) adhered to the grains' surfaces of TV.

For the representative semi-graphite sample BC (R_{max} = 5.39%). The newly formed MDC now includes matrix graphite, flake graphite, and crystalline aggregates. In the semi-graphite, the pyrolytic carbon deposits on the edge of matrix graphite, forming a graphite shell (Fig. 7(a)). The shells' void cavities are filled with crystalline tar (Fig. 7(b)). The flake graphite is distributed in the matrix graphite fractures along with the crystalline aggregates (Figs. 7(c)–7(d)). The flake graphite was formed as a result of the further crystallization of the crystalline tar. In comparison with the meta-anthracite, the matrix graphite takes up the biggest share of all MDC while more thermoplastic vitrinite is no longer visible.

In the representative CDNG sample (PSZK), most of the MDCs are similar to that of semi-graphite. However, the flake graphite (Figs. 7(e)–7(f)) takes the place of crystalline tar with further crystallization. The crystalline aggregates also take a larger share than that in semi-graphite. Figure 7(g) shows the SEM image of the surface of matrix graphite, the matrix graphite particles were present on the surface of lump graphite. Figure 7(h) shows the graphite basal plane (GBP) of matrix graphite. Some graphite particles show a rough hexagon shape, as a highly ordered graphite structure is attained, it represents the property of self-confinement. Figures 7(e) –7(f) exhibit the graphite edge plane, the graphite particles represent a thin sheet with heights of about 50 nm, which is consistent with the L_c value calculated by XRD (Table 2). However, these graphite sheets do not stack parallelly in a long range because of the existence of structural defects.

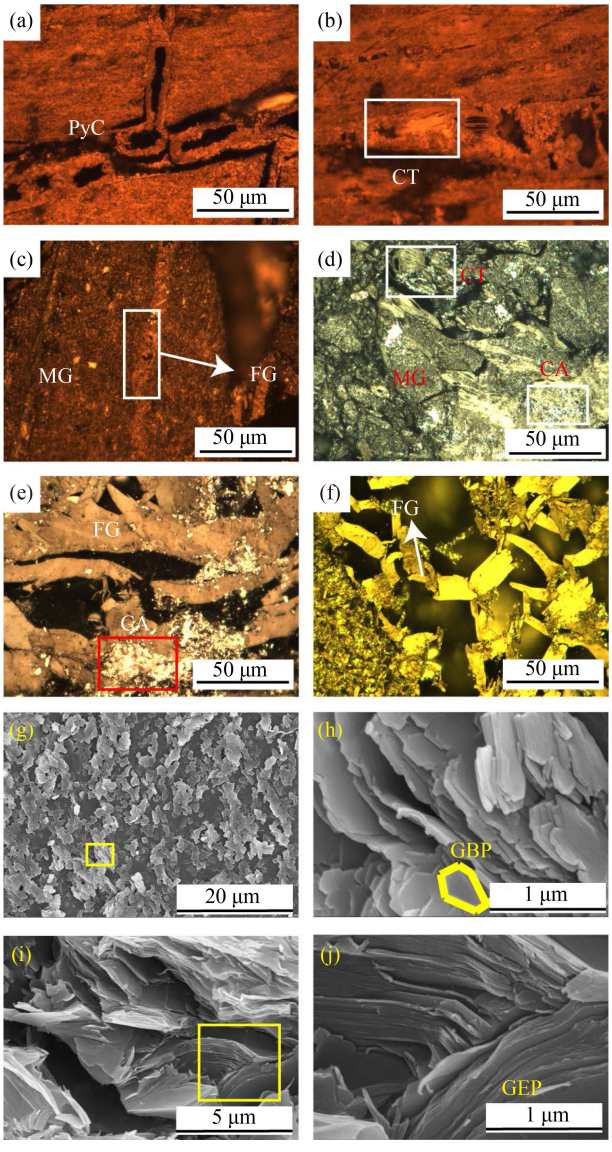

Fig. 7 Representative photomicrographs and SEM of samples. For optical observation, the images were taken under polarized light, × 50 anti-reflective objective, under oil immersion. (a) PyC and Matrix graphite (MG) in semi-graphite; (b) flake graphite (FG) and MG in semi-graphite; (c) PyC, CT, and MG in semi-graphite; (d) MG, CT, and crystalline aggregates (CA) in CDNG; (e) and (f) FG and CA in CDNG. (g) MG under SEM in CDNG; (h) graphite basal plane (GBP); (i) and (j) graphite edge plane (GEP) under SEM in CDNG.

4.4 Micro-Raman analyses

4.4.1 Microstructural structural evolution as detected by micro-Raman spectroscopy

The representative micro-Raman spectra and the peak-fitting pattern were shown in Fig. 8 and the quantized data of Raman parameters were shown in Table 3. For the anthracite sample CM (Fig. 8(a)), the Raman pattern of the "normal" vitrinite shows a typical coal Raman pattern with well-separated D1, D3, and D4 peaks, also with two broad peaks in the second peak region (around 2700 cm^{-1} and 3240 cm^{-1}). The I_{D1}/I_{D2} (R1) and R2 values were used to evaluate the structural ordering degree, lower R1 and R2 values mean a higher structural ordering degree for carbonaceous materials (Li et al., 2020b; Potgieter-Vermaak et al., 2011; Tuinstra and Koenig, 1970; Xu et al., 2017). While for the "normal" macerals, the R1 and R2 values are both smaller than altered macerals or MDCs which is contrary to expectations. The thermoplastic vitrinite (Fig. 8(b)) shows a different pattern to the "normal" macerals with board D1, D4, and G peaks but the D3 peak was not present. The disappearance of the D3 peak indicated that the aliphatic chain was reduced.

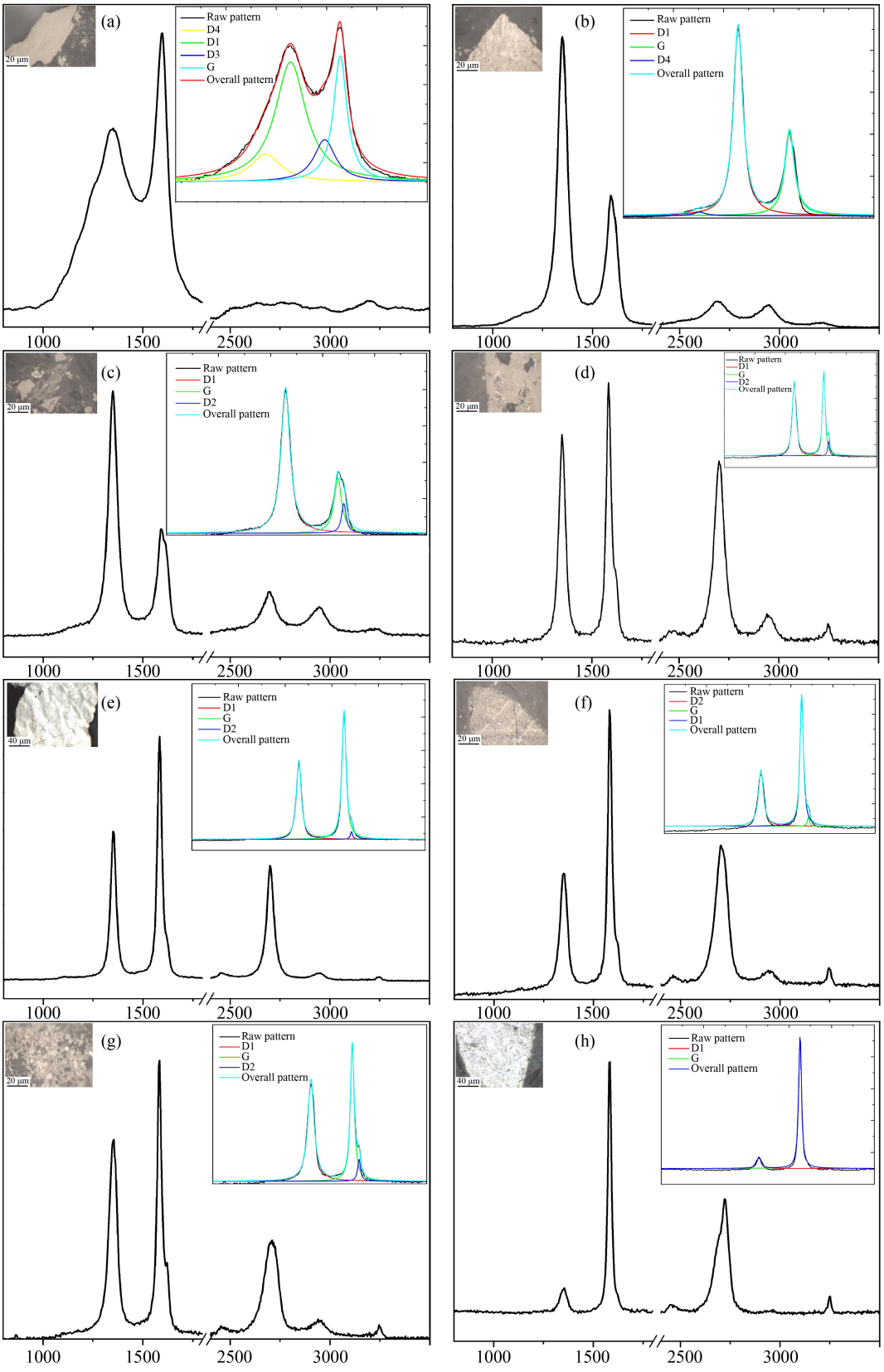

Fig. 8 Representative micro-Raman patterns and peak-fitting patterns of the first-order region of the maceral/MDCs. (a) "Normal" vitrinite; (b) TV; (c) D-V; (d) CT in vacuoles; (e) MS; (f) MG; (g) FG and (h) CA. The *X*-axis is Raman shift (cm^{-1}) and the *Y*-axis is intensity (a.u).

Table 3 Detailed micro-Raman parameters of selected samples

Samples	Components	D4		D1		D3		G		D2		R1	R2
		FWHM	Position	FWHM	Position	FWHM	Position	FWHM	Position	FWHM	Position		
CM	DT	198 (3.30)	1240 (4.85)	252 (2.73)	1337 (4.43)	92 (1.34)	1555 (6.51)	59 (7.52)	1594 (9.06)			0.86	0.14
	TV	73 (4.45)	1186 (8.08)	77 (7.45)	1344 (5.38)			49 (6.29)	1587 (9.35)			1.27	0.67
	D-V			49 (1.07)	1349 (0.89)			41 (2.69)	1590 (7.24)	25 (9.35)	1618 (1.34)	2.64	0.70
SL	MS			35 (0.75)	1350 (3.53)			26 (2.93)	1583 (9.87)	15 (3.38)	1622 (5.21)	0.59	0.43
	CT			37 (8.42)	1351 (1.56)			26 (7.08)	1582 (8.27)	14 (5.43)	1623 (7.96)	0.28	0.28
BC	PyC			40 (8.39)	1351 (1.41)			24 (1.68)	1584 (5.59)	20 (0.81)	1619 (9.74)	1.67	0.60
	CT			36 (2.18)	1351 (2.66)			26 (7.84)	1584 (4.73)	15 (3.61)	1622 (5.35)	0.89	0.53
	CA			33 (5.49)	1353 (9.51)			21 (7.85)	1582 (5.41)	5 (8.71)	1624 (4.27)	0.19	0.22
	MG			32 (5.07)	1351 (7.75)			26 (1.34)	1583 (9.44)	13 (2.25)	1622 (7.72)	0.73	0.46
SXL	CA			29 (1.88)	1353 (2.13)			24 (6.02)	1582 (1.90)			0.15	0.16
	MG			34 (8.76)	1350 (4.46)			23 (5.31)	1582 (4.06)	13 (3.84)	1620 (4.28)	0.42	0.38
PSXRD	CA			32 (2.77)	1349 (9.87)			22 (3.66)	1582 (6.41)	9 (7.60)	1622 (0.36)	0.28	0.29
	FG			41 (0.49)	1351 (6.06)			26 (4.11)	1583 (5.06)	17 (6.45)	1622 (4.68)	0.76	0.52
PSZK	CA			29 (3.32)	1351 (6.95)			17 (8.79)	1583 (1.93)	11 (0.71)	1623 (1.55)	0.27	0.30
	FG			46 (5.69)	1352 (9.88)			26 (5.33)	1583 (0.15)	17 (2.81)	1623 (8.22)	0.66	0.57
NF63	FG			42 (8.41)	1351 (3.73)			25 (9.65)	1583 (8.05)	20 (0.36)	1621 (0.81)	0.74	0.52
	CA			32 (1.41)	1349 (2.57)			21 (4.86)	1582 (3.76)	6 (1.71)	1620 (1.58)	0.26	0.28
NF68	FG			44 (6.99)	1350 (5.13)			27 (5.96)	1582 (3.63)	20 (6.91)	1621 (0.66)	0.90	0.56
	CA			33 (0.22)	1351 (6.06)			22 (8.69)	1582 (0.73)	8 (0.97)	1621 (0.12)	0.21	0.24
NF617	FG			42 (6.46)	1354 (0.16)			28 (1.91)	1584 (2.62)	21 (2.80)	1623 (8.18)	0.90	0.60
	CA			29 (0.47)	1351 (1.14)			21 (3.63)	1582 (2.11)			0.06	0.08

Notes: DT is desmocollinite; TV is thermoplastic vitrinite; D-V is devolatilized vitrinite; MS is mosaic structure; CT is crystalline tar; PyC is pyrolytic carbon; CA is crystalline aggregates; MG is matrix graphite; and FG is flake graphite. The R1=D1/D2 intensity ratio. The R2=D1/(D1 + D2 + G) area ratio. The standard deviation is in the brackets after data

The G peak is also asymmetrical. In the second peak region, the 2D1, D1 + G, and 2D2 peaks were present. For the D-V (Fig. 8(c)), the D4 peak disappears, while the well-separated D2 peak occurs, indicating that a higher metamorphic degree is achieved.

For the meta-anthracite sample SL, the micro-Raman pattern of crystalline tar was shown in Fig. 8(d). The D1, G, and D1 + G peaks are present along with a D2 band that occurs in the right shoulder of the G band in the first-order region. The $2D_R$, 2D1, D1 + G, and 2D2 are observed as well. The mosaic structure (Fig. 8(e)) usually occurs in the meta-anthracite. The low R1 (0.59) and R2 (0.43) values indicated that the mosaic structure has a high structural ordering value. The $2D_R$ peak occurs indicated a large aromatic ring system is formed (Xu et al., 2017).

For the semi-graphite and CDNG sample, the matrix graphite, flake graphite, and crystalline aggregates were shown in Figs. 8(f)–8(h), respectively. The flake graphite (Fig. 8(g)) shows a quite similar Raman pattern with the crystalline tar. Per the Figs. 7(b)–7(d), it can be inferred that the tar gradually fills and crystallizes in the void cavities, ultimately forming flake graphite. The flake graphite is less ordered with R2 value > 0.4, R1 value > 0.5 than the crystalline aggregates. The Raman pattern also shows that these flake graphite particles are equivalent to the GEP of natural graphite per previous research (Rodrigues et al., 2013). The crystalline aggregates exhibit the highest structural ordering degree with R2 = 0.22 and G-FWHM = 21 cm^{-1}. Additionally, the D1 + G peak began to split and the 2D2 peak is much weaker, which also indicated the triperiodical graphite structure is achieved. These Raman characteristics also correspond to the GBP per the previous report on natural graphite (Rodrigues et al., 2013), which revealed that the crystalline aggregates are GBP indeed. For the matrix graphite, the peak shape shows no significant difference with flake graphite except for the intensity. A quantity of data are needed to distinguish them.

Here, the crystalline aggregates and crystalline tar coexist within the same MDC particle void cavities in the same MDC (Fig. 9), suggesting that crystalline tar and crystalline aggregates formed under the similar temperature and stress condition. Their differences in optical and micro-Raman spectra may be due to the orientation of the crystal plane. As crystalline tar is the

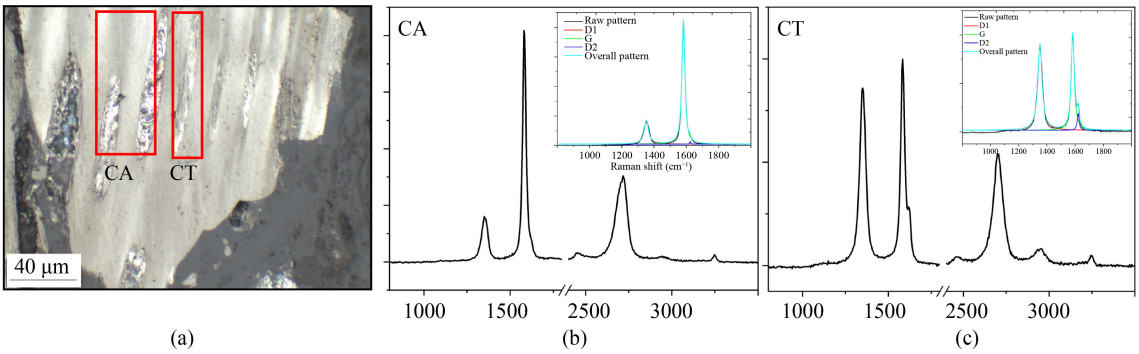

Fig. 9 Crystalline aggregates and CTs within the same MDC particle and their micro-Raman pattern.

main precursor of flake graphite, flake graphite is GEP. The crystalline aggregate is GBP.

Graphitization in coal begins at the semi-anthracite and continues through anthracite and meta-anthracite ranks, ultimately (with the right conditions) leading to semi-graphite and graphite (Li et al., 2018). While graphitization *sensu stricto* consists mostly of polymerizations and structural rearrangement of the aromatic skeleton toward the thermodynamically stable ABAB layered sequence of graphite (Buseck and Beyssac, 2014); the transformation from semi-anthracite to semi-graphite is also called carbonization. An empirical plot of the D1-FWHM versus R1 (Fig. 10) was used to discriminate the carbonization and graphitization. The components in graphitization usually have an R1 value < 1.5 and D1-FWHM value < 50 cm^{-1}. The crystalline tar, mosaic thermoplastic maceral, flake graphite, and crystalline aggregates are all in graphitization (Fig. 9).

4.5 Coal natural graphitization

Based on the bulk characterization, morphological feature, and micro-Raman data. It can be inferred there may be three kinds of natural graphitization phases, namely in situ solid-state transformation (solid-phase), gas-phase (pyrolytic carbon conversion), and liquid-phase (crystalline tar transformation). The *in situ* solid-state transformation refers to the macerals transformation without migration; the macerals were heated by magma and massive gas precipitation (volatile) thus presents a mosaic structure (Fig. 6(b)), similar to that of natural coke. These mosaic structures are usually found in the meta-anthracite. With graphitization, the granular structure within the maceral becomes dense thus forming the matrix graphite. The pyrolytic carbon are the deposits formed on a hot substrate by the dehydrogenation of a gaseous hydrocarbon. Pyrolytic carbon was formed due to the chemical cracking of volatiles produced by the thermally altered macerals. In comparison with the pyrolytic carbon in laboratories, this pyrolytic carbon in natural graphitization also shows small spheres but have a much smaller size (Figs. 6(e)–6(f)) (20–40 nm) than the previous reports (1–10 μm) under SEM. Under the optical microscope, the pyrolytic carbon lies in the edge of macerals (Fig. 7(a)), matrix graphite or fill in the cell cavities, exhibiting a shell shape. The crystallin tar were found in the meta-anthracite and semi-graphite. They usually filled in fracture and void cavities (Figs. 6(b)–6(d), and 7(b)). The macerals were altered thus present a flow structure. Coal tar precipitates and crystallizes in the cavities.

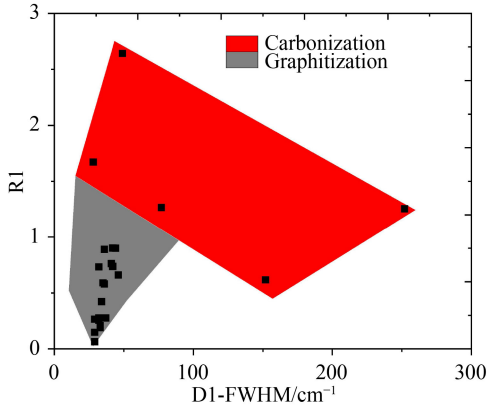

Fig. 10 A plot of D1-FWHM versus R1 (Rouzaud et al., 2015).

5 Conclusions

Based on the bulk characterization (geochemistry, XRD, and powder Raman spectroscopy), in Xinhua, the d_{002} decreases while the L_a, L_c, and N_{ave} increase as the distance to granitic pluton decrease. However, in a region with a big granitic mass that can provide sufficient heat, the distance impacts slightly. A further decrease of the distance results only in a minor decrease of the d_{002} value. However, the d_{002} decrease is not continuous due to shear stress. Per the d_{002} data, the metamorphic degree of the CDNG sample in the Panshi region is the highest. After entering graphitization, R2 and *AI* have a better correlation with d_{002}.

The thermoplastic vitrinite, devolatilized vitrinite, and some “normal” macerals were present on the anthracite. While the crystalline tar, pyrolytic carbon, and mosaic

structure were present on the meta-anthracite. In semi-graphite and CDNG, the matrix graphite, flake graphite, and crystalline aggregates are the newly formed MDCs. The thermoplastic vitrinite exhibit a weak optical anisotropy while the devolatilized shows a reticular structure, the "normal" macerals were composed of some desmocollinite. The crystalline tar shows a fluid state in some void cavities, the pyrolytic carbon lies in the edges of the brecciated fragments, while the mosaic structure lacks a clear outline between other macerals or MDCs. The matrix graphite was present on the surface of lump graphite and takes the dominant position of all MDCs. The flake graphite is distributed in the matrix graphite fractures along with the crystalline aggregates. Based on the micro-Raman pattern and quantified data. In anthracite, the D1, D3, D4, and G peaks were present, while the D3 peak disappears in thermoplastic vitrinite. In the devolatilized vitrinite, the D4 peak disappear while the D2 peak occurs in the shoulder of G peak. The pyrolytic carbons, and crystalline tar present a similar Raman pattern but different Raman parameters in the meta-anthracite sample. Per the Raman parameter, the pyrolytic carbon shows the highest structural ordering degree among the three kinds of particles. The crystalline aggregates, matrix graphite, flake graphite along with some Pyrolytic carbon, and CT were found in CDNG. The crystalline aggregates show the highest structural ordering degree with G-FWHM of about 20 cm^{-1}, R2 < 0.5. The flake graphite is less ordered with its G-FWHM of about 28 cm^{-1}, 0.5 < R2 < 1, but a larger size up to 50 μm. Per the micro-Raman data and direct observation, the flake graphite and crystalline are GEP and GBP, respectively.

Based on these features, three kinds of graphitization approaches can be summarized: the *in situ* solid-state transformation, pyrolytic carbon conversion, and crystalline tar transformation. The *in situ* solid state transformation refers to the thermoplastic mosaic macerals to the matrix graphite, the pyrolytic carbon and crystalline tar conversion refer to the gas-phase and liquid-phase transformation.

Acknowledgments This work is supported by the National Natural Science Foundation of China (Grant Nos. 41672150 and 42002187) and the Scholarship from the China Scholarship Council (No. 201906430017).

Electronic supplementary material is available in the online version of this article at http://dx.doi.org/10.1007/s11707-021-0967-4 and is accessible for authorized users.

References

Bai D Y, Huang J Z, Liu Y R, Wu G Y, Wang X H, (2005). Framework of mesozoic tectonic evolution in southeastern Hunan and the Hunan-Guangdong-Jiangxi border area. Chin Geol, 32(4): 566−570

Beyssac O, Rumble D (2014). Graphitic carbon: a ubiquitous, diverse, and useful geomaterial. Elements, 10(6): 415–420

Blanche C C, Rouzaud J N, Dumas D (1995). New data on anthracite graphitizibility

Bonijoly M, Oberlin M, Oberlin A (1982). A possible mechanism for natural graphite formation. Int J Coal Geol, 1(4): 283–312

Buseck P R, Beyssac O (2014). From organic matter to graphite: Graphitization. Elements, 10(6): 421–426

Buseck P R, Huang B J (1985). Conversion of carbonaceous material to graphite during metamorphism. Geochim Cosmochim Acta, 49(10): 2003–2016

Bustin R M, Ross J V, Rouzaud J N (1995). Mechanisms of graphite formation from kerogen: experimental evidence. Int J Coal Geol, 28(1): 1–36

Chao L I, Wang D H, Zhou L M, Zhao H, Li X W, Qu W J (2017). Study on the Re-Os isotope composition of graphite from the Lutang graphite deposit in Hunan Province. Rock and Mineral Analysis

Duber S, Rouzaud J N, Bény C, Dumas D (1993). Graphitization of anthracites

Eckmann A, Felten A, Mishchenko A, Britnell L, Krupke R, Novoselov K S, Casiraghi C (2012). Probing the nature of defects in graphene by Raman spectroscopy. Nano Lett, 12(8): 3925–3930

González D, Montes-Morán M A, Garcia A B (2003). Graphite materials prepared from an anthracite: a structural characterization. Energy Fuels, 17(5): 1324–1329

Goodarzi F, Eckstrand O R, Snowdon L, Williamson B, Stasiuk L D (1992). Thermal metamorphism of bitumen in archean rocks by ultramafic volcanic flows. Int J Coal Geol, 20(1): 165–178

Guedes A, Valentim B, Prieto A C, Noronha F (2012). Raman spectroscopy of coal macerals and fluidized bed char morphotypes. Fuel, 97: 443–449

Guedes A, Valentim B, Prieto A C, Rodrigues S, Noronha F (2010). Micro-raman spectroscopy of collotelinite, fusinite and macrinite. Int J Coal Geol, 83(4): 415–422

Han Y Z, Xu R T, Hou Q L, Wang J, Pan J N (2016). Deformation mechanisms and macromolecular structure response of anthracite under different stress. Energ Fuel, 30(2): 975–983

Harris P J F (2005). New perspectives on the structure of graphitic carbons. Crit Rev Solid State Mater Sci, 30(4): 235–253

Hinrichs R, Brown M T, Vasconcellos M A Z, Abrashev M V, Kalkreuth W (2014). Simple procedure for an estimation of the coal rank using micro-Raman spectroscopy. Int J Coal Geol, 136: 52–58

Hower J C, O'Keefe J M K, Valentim B, Guedes A (2021a). Contrasts in maceral textures in progressive metamorphism versus near-surface hydrothermal metamorphism. Int J Coal Geol, 246: 103840

Hower J C, Rimmer S M, Mastalerz M, Wagner N J (2019). Notes on the mechanisms of coal metamorphism in the Pennsylvania anthracite fields. Int J Coal Geol, 202: 161–170

Hower J C, Rimmer S M, Mastalerz M, Wagner N J (2021b). Migmatite-like textures in anthracite: further evidence for low-grade metamorphic melting and resolidification in high-rank coals. Geosci Front, 12(3): 101122

Kuo L W, Li H B, Smith S A F, Di Toro G, Suppe J, Song S R, Nielsen S, Sheu H S, Si J L (2014). Gouge graphitization and dynamic fault

weakening during the 2008 MW 7.9 Wenchuan earthquake. Geology, 42(1): 47–50

Kwiecińska B, Petersen H I (2004). Graphite, semi-graphite, natural coke, and natural char classification—ICCP system. Int J Coal Geol, 57(2): 99–116

Kwiecinska B, Suarez-Ruiz I, Paluszkiewicz C, Rodrigues S (2010). Raman spectroscopy of selected carbonaceous samples. Int J Coal Geol, 84(3−4): 206–212

Kwiecińska B K, Pusz S (2016). Pyrolytic carbon—definition, classification and occurrence. Int J Coal Geol, 163: 1–7

Li K (2019). Investigation on the structural ordering of natural coaly graphite from Xinhua, Hunan Province, China. Dissertation for Doctoral Degree. Beijing: China University of Mining and Technology

Li K, Liu Q, Rimmer S M, Huggett W W, Zhang S (2020a). Investigation of the carbon structure of naturally graphitized coals from central Hunan, China, by density-gradient centrifugation, X-ray diffraction, and high-resolution transmission electron microscopy. Int J Coal Geol, 232: 103628

Li K, Liu Q F, Hou D D, Wang Z G, Zhang S (2021). Quantitative investigation on the structural characteristics and evolution of high-rank coals from Xinhua, Hunan Province, China. Fuel, 289: 119945

Li K, Rimmer S M, Liu Q F (2018). Geochemical and petrographic analysis of graphitized coals from central Hunan, China. Int J Coal Geol, 195(April): 267–279

Li K, Rimmer S M, Liu Q F, Zhang Y M (2019). Micro-Raman spectroscopy of microscopically distinguishable components of naturally graphitized coals from central Hunan Province, China. Energ Fuel, 33(2): 1037–1048

Li K, Rimmer S M, Presswood S M, Liu Q F (2020b). Raman spectroscopy of intruded coals from the Illinois basin: correlation with rank and estimated alteration temperature. Int J Coal Geol, 219: 103369

Lu L, Sahajwalla V, Kong C, Harris D (2001). Quantitative X-ray diffraction analysis and its application to various coals. Carbon, 39(12): 1821–1833

Nemanich R J, Solin S A (1979). First- and second-order Raman scattering from finite-size crystals of graphite. Phys Rev B Condens Matter, 20(2): 392–401

Nyathi M S, Clifford C B, Schobert H H (2013). Characterization of graphitic materials prepared from different rank Pennsylvania anthracites. Fuel, 114: 244–250

Oberlin A (1984). Carbonization and graphitization. Carbon, 22(6): 521–541

Oberlin A (2002). Pyrocarbons. Carbon, 40(1): 7–24

Oberlin A, Terriere G (1975). Graphitization studies of anthracites by high resolution electron microscopy. Carbon, 13(5): 367–376

Potgieter-Vermaak S, Maledi N, Wagner N, Van Heerden J H P, Van Grieken R, Potgieter J H (2011). Raman spectroscopy for the analysis of coal: a review. J Raman Spectrosc, 42(2): 123–129

Rantitsch G, Lämmerer W, Fisslthaler E, Mitsche S, Kaltenböck H (2016). On the discrimination of semi-graphite and graphite by Raman spectroscopy. Int J Coal Geol, 159: 48–56

Robinson G R Jr, Hammarstrom J M, Olson D W, Robinson G R Jr, Hammarstrom J M, Olson D W (2017). Graphite. 1802J, Reston: VA

Rodrigues S, Marques M, Suarez-Ruiz I, Camean I, Flores D, Kwiecinska B (2013). Microstructural investigations of natural and synthetic graphites and semi-graphites. Int J Coal Geol, 111: 67–79

Rouzaud J N, Deldicque D, Charon E, Pageot J (2015). Carbons at the heart of questions on energy and environment: a nanostructural approach. C R Geosci, 347(3): 124–133

Schwan J, Ulrich S, Batori V, Ehrhardt H, Silva S R P (1996). Raman spectroscopy on amorphous carbon films. J Appl Phys, 80(1): 440–447

Tuinstra F, Koenig J L (1970). Raman spectrum of graphite. J Chem Phys, 53(3): 1126–1130

Wang L, Cao D Y, Peng Y W, Ding Z Y, Li Y (2019a). Strain-induced graphitization mechanism of coal-based graphite from Lutang, Hunan Province, China. Minerals (Basel), 9(10): 1–19

Wang L, Qin R F, Li Y, Zhang H, (2019b). On the difference of graphitization behavior between vitrinite- and inertinite-rich anthracites during heat treatment. Energ Source: 7036

Wang Y, Ma S, Shimamoto T, Yao L, Chen J, Yang X, He H, Dang J, Hou L, Togo T (2014). Internal structures and high-velocity frictional properties of Longmenshan fault zone at Shenxigou activated during the 2008 Wenchuan earthquake. Earth Sci (Paris), 27(5): 499–528

Wu Y, Li K, Wang Z, Hu M, Cao H, Liu Q (2021). Fluctuations in graphitization of coal seam-derived natural graphite upon approaching the Qitianling granite intrusion, Hunan, China. Minerals (Basel), 11(10): 1147

Xu J, Tang H, Su S, Liu J W, Han H D, Zhang L P, Xu K, Wang Y, Hu S, Zhou Y B, Xiang J (2017). Micro-Raman spectroscopy study of 32 kinds of Chinese coals: second-order raman spectrum and its correlations with coal properties. Energ Fuel, 31(8): 7884–7893

Yuan L, Liu Q F, Mathews J P, Zhang H, Wu Y K (2021). Quantifying the structural transitions of Chinese coal to coal-derived natural graphite by XRD, Raman spectroscopy, and HRTEM image analyses. Energ Fuel, 35(3): 2335–2346

Zhang S, Liu Q F, Zhang H, Ma R J, Li K, Wu Y K, Teppen B J (2020). Structural order evaluation and structural evolution of coal derived natural graphite during graphitization. Carbon, 157: 714–723

Zheng Z, Zhang J, Huang J Y (1996). Observations of microstructure and reflectivity of coal graphites for two locations in China. Int J Coal Geol, 30(4): 277–284

Zhu J, Wang R, Zhang P, Xie C, Zhang W, Zhao K, Xie L, Yang C, Che X, Yu A, Wang L (2009). Zircon U-Pb geochronological framework of Qitianling granite batholith, middle part of Nanling range, south China. Sci China Ser D Earth Sci, 52(9): 1279–1294